

Chitin Matrix and Ultrastructure of Phosphate-Shelled Brachiopods

Oluwatoosin Agbaje (✉ toosin.agbaje@mq.edu.au)

Macquarie University

Glenn Brock

Macquarie University

Zhifei Zhang

Northwest University

Yue Liang

Northwest University

Simon George

Macquarie University

Lars Holmer

Uppsala University

Research Article

Keywords: microRaman spectroscopy, chitin, fibrous proteins, biomineralization, spatial ultrastructure

Posted Date: December 17th, 2020

DOI: <https://doi.org/10.21203/rs.3.rs-129606/v1>

License:  This work is licensed under a Creative Commons Attribution 4.0 International License.

[Read Full License](#)

1 **Chitin matrix and ultrastructure of phosphate-shelled brachiopods**

2 **Oluwatoosin B. A. Agbaje,^{a,b,c*} Glenn A. Brock,^{c,d} Zhifei Zhang,^d Yue Liang,^d Simon C.**
3 **George,^b Lars E. Holmer^{a, d}**

4 ^a Department of Earth Sciences, Palaeobiology, Uppsala University, Uppsala, Uppsala,
5 Sweden

6 ^b Department of Earth and Environmental Sciences and MQ Marine Research Centre,
7 Macquarie University, Sydney, Australia.

8 ^c Department of Biological Sciences, Macquarie University, Sydney, Australia.

9 ^d State Key Laboratory of Continental Dynamics, Shaanxi Key Laboratory of Early Life &
10 Environments, Department of Geology, Northwest University, Xi'an, 710069, China.

11
12 * **Correspondence:** toosin.agbaje@mq.edu.au; toosin91014@gmail.com

13
14 **Abstract**

15
16 Phosphate-shelled brachiopods differ in filter-feeding life style, with *Lingula anatina* an active
17 infaunal burrower, and *Discinisca tenuis* a shallow marine epibenthic animal. The shells of
18 these biomineralized organisms are built of organophosphatic constituents, the organic
19 fibres/sheets reinforced with calcium phosphate (Ca-phosphate) to provide a sophisticated
20 ultrastructural robustness. This investigation studied the nature of organic fibres in order to
21 improve our understanding of how design principles are relevant to biominerals. Unlike the
22 powdered samples that were commonly used in previous studies, for the first time organic
23 fibres were isolated and the shell fractions were purified, in order to study the content and
24 nature of the biopolymer fibres. Ultrastructural analysis, thermal gravimetric analysis and
25 spectroscopic analyses reveal that the core polysaccharide framework is composed of layers of
26 β -chitin sheets that are coated with a fibrous protein matrix. The chitin matrix in *Lingula* shells,
27 26.6 wt.%, is about two-fold higher wt.% compared to *Discinisca* shells, 12.9 wt.%. After
28 thermal gravimetric analysis, skeletal imaging of these shells shows important differences.
29 *Discinisca* contains just a single layer that is ~21.0 μm thick. In contrast, *Lingula* exhibits two
30 separate layers: the thicknesses of the primary- and secondary-layers are ~20.3 μm and ~8.1

31 μm , respectively. Taken together, the data shows that the chitin matrix contributes to increased
32 skeletal strength, making *Lingula* highly adapted for life as an active burrower. In comparison,
33 *Discinisca* contains less chitin and lives as attached epibenthos in a shallow marine
34 environment.

35 **Keywords:** microRaman spectroscopy; chitin; fibrous proteins; biomineralization; spatial
36 ultrastructure

37 **Introduction**

38 Biominerals such as seashells, teeth or bones are produced by living organisms and formed
39 into functional architectures under natural selection, typically as inorganic-organic
40 nanocomposites. Inorganic matrices comprise calcium carbonates and phosphates, whereas
41 organic macromolecules constitute a combination of soluble- and insoluble-organic
42 components, primarily protein and polysaccharide layers which provide a scaffolding for the
43 inorganic phase^{1,2}. Water insoluble macromolecules are most frequently built from monomers
44 based either on sugars or peptides^{3,4}. Sugar monomers and biomolecules based on peptides are
45 present throughout the animal kingdom². The former are chemically modified most commonly
46 by amination, and are referred to as chitin or chitosan, depending largely on the degree of
47 subsequent deacetylation^{2,5}. However, biomolecules based on peptides can either be functional
48 or structural proteins comprised of a variety of fibrous, tubular and collagen triple helices³. In
49 the matrix sheets of shell biominerals, the core polysaccharide framework is composed of the
50 interlamellar structure of β -chitin, and is frequently reinforced and/or composited with
51 extracellular matrix², other biomolecules include glycosaminoglycans^{6,7} and/or inorganic
52 matrices⁸. These composite materials are high-strength yet lightweight, and provide functional
53 flexibility, support ultrastructures, mechanical stability and compressive strength^{4,8,9}. The
54 composition of organic-inorganic matrices form extraordinary arrays of diverse biomineralized
55 ultrastructures which eventually facilitate adaptation to a diverse suite of habitats^{10,11}.

56 Brachiopods are a diverse group of marine, sessile and benthic filter-feeding lophophorate
57 animals that are categorised into three subphyla: Linguliformea, Craniiformea and
58 Rhynchonelliformea¹². Craniiformea and Rhynchonelliformea utilize calcitic calcium
59 carbonate and organic constituents, about 2%, to hierarchically assemble ultrastructures of the
60 shell¹³. In contrast, linguliform brachiopods such as *Lingula* and *Discinisca* use organic
61 biopolymers reinforced with Ca-phosphate to produce the shell (e.g.¹⁴). The shell biominerals
62 of Linguliformea consist of carbonate-substituted fluorapatite ($\text{Ca}_{10}(\text{PO}_4)_6\text{F}_2$; francolite) and
63 originated some 530 million years ago in the early Cambrian as part of the emergence of
64 biomineralization across disparate animal clades^{12,15}. These biominerals exhibit distinctive
65 features including ciliated lophophores, chitinous setae, as well as a tail-like pedicle for
66 anchoring to (or within) the substrate^{12,16}. Typical *Discinisca* uses a muscular pedicle for
67 attachment to hard substrates, so as to survive wave action in the steeper slopes of the shallow
68 seafloor¹⁰. In contrast, *Lingula* uses a pedicle to prop itself up with the shell against the
69 sediment. The downward U-shaped burrowing is accomplished by cyclical complex motions
70 of the valves against the sediment, with the pedicle trailing behind the shell^{10,11,16-18}. Definitive
71 evidence for an active U-shaped burrowing lingulid lifestyle is unknown from the Palaeozoic,
72 where the obolids burrowed pedicle first¹⁶⁻¹⁸; the first appearance of the U-shaped burrows
73 likely occurred during the Mesozoic; it may have been connected with the de-mineralization
74 and more flexible shell that have been discussed here for the survival of Lingulidae, against the
75 erosion of the substrate since the early Palaeozoic^{10,16-18}.

76 Linguliform shells are used as paleoenvironmental proxies due to their enviably complete fossil
77 record and their sporadic distribution in modern oceans^{12,19}. Despite their palaeontological
78 importance, the growth mechanism of brachiopod shells is not clearly understood, and
79 regarding the key components of organic biopolymers, detailed structural and molecular
80 analyses are of great interest. Although biochemical studies and spectroscopic analyses on

81 powdered brachiopod samples have identified proteins associated with chitin from linguliform
82 shells (e.g.^{6,20,21}), the composite fibres have not been characterised, so little is known about the
83 nature of the organic sheets. Chemical fixation and scanning electron microscopy (SEM) were
84 used to propose that the organic fibrils in linguliform shells are composed of chitin, a dense
85 mat of fibrils which are probably collagenous, and membranous laminae within the shell layers
86 ^{7,22}. However, these previous studies were based on a more or less complete mixture of organic
87 biopolymers and Ca-phosphate mineral. It is necessary to establish an easy and fast method to
88 reveal the composition of the organic sheet layers in brachiopod shells. The approach of this
89 study is to use field emission gun-SEM (FEG-SEM), and comparison of the imaged region
90 with the natural composite biominerals analysed by microRaman spectroscopy and Fourier
91 transform infrared (FTIR) spectroscopy. This study had two main goals: firstly to identify the
92 major organic frameworks in lingulid shells, and secondly to determine the skeletal formation
93 and components of the shell biominerals. This investigation is of interest for understanding the
94 morphological structures of fossilised, recent and modern phosphate-shelled brachiopods and
95 the biosynthesis of organic-inorganic composites, and for the design of skeletal structures of
96 new materials. Also, this study provides direct evidence on skeletal biomineral evolutionary
97 adaptations of active burrowing and epibenthic lingulids for their different habitats.

98 **Results**

99 **Vibrational spectroscopy – microRaman and FTIR spectra**

100 Raman spectra of organic fibres from the shell samples (**Fig. 1**) show absorption bands that are
101 typical of chitin (*N*-acetyl-D-glucosamine). The band assignments are listed in **SI Table 1** and
102 are compared with the spectrum of standard α -chitin and the literature ²³⁻²⁶. The spectra of the
103 organic fibres reveal the presence of C=O (carbonyl) functional groups based on the amide I
104 stretching vibration at $\sim 1654\text{ cm}^{-1}$, and correspond primarily to the β -form of chitin. The

105 deconvolutional fit of the amide I band in the 1580–1720 cm^{-1} range (**SI Fig. 1**) has some
106 ubiquitous features with that of standard α -chitin, but the vibrational bands have different area
107 percentages (**SI Table 2**). The rocking CH_2 vibrations at 1376 cm^{-1} and the amide III bands in
108 the 1202–1327 cm^{-1} range are predominantly assigned to organic biopolymers (**Fig. 1**). The
109 CH deformation of the β -glycosidic bond band at 897 cm^{-1} for *D. tenuis* and at ~ 902 cm^{-1} for
110 *L. anatina* is present at 895 cm^{-1} in standard α -chitin. Bands at 1003 cm^{-1} in *L. anatina* and
111 1005 cm^{-1} in *D. tenuis* are not present in standard α -chitin and are attributed to the aromatic C-
112 C stretch of fibrous insoluble protein²⁷⁻²⁹. The vibrational bands at ~ 856 cm^{-1} and ~ 820 cm^{-1}
113 are assigned to a combination of C-C and C-O stretching, and appear in *L. anatina* only. Ca-
114 phosphate vibrational bands at 964 cm^{-1} , 608 cm^{-1} and 581 cm^{-1} are only present in the *D. tenuis*
115 spectrum (**Fig. 1**; **SI Fig. 2**). An attempt to completely remove inorganic components to expose
116 the chitin framework in *D. tenuis* proved unsuccessful, because the organic macromolecules
117 were completely removed during the extraction and purification stages, instead of the inorganic
118 matrix. This was most likely due to the fact that both Ca-phosphate and the framework of
119 organic biopolymers form complexes to produce shell ultrastructure.

120 FTIR spectroscopy was used to probe and/or identify the molecular and functional properties
121 of the organic fibres from the shell samples, and used for comparison the α -chitin standard
122 (**Fig. 2**). The amide I of the insoluble matrix shows a broad band with a partial splitting pattern
123 in two bands at 1646–1652 cm^{-1} and 1630–1635 cm^{-1} , while standard α -chitin has two bands at
124 1656 cm^{-1} and 1621 cm^{-1} . The spectra at 1550 cm^{-1} (Amide II), in the range 1203–1308 cm^{-1}
125 (Amide III), and the stretching C-O bands in the 1153–950 cm^{-1} range (**Fig. 1**; **SI Fig. 2**) are
126 indicative of chitin. The fingerprint region of the organic fibres of the phosphate-shelled
127 brachiopods are doublet bands at 702–708 cm^{-1} and 691–692 cm^{-1} , suggesting crystalline chitin.
128 The stretching band of the OH group for shell samples is centred at ~ 3424 cm^{-1} , with a shoulder
129 near 3532 cm^{-1} . Other spectra bands for amide A (3282–3272 cm^{-1}), amide B (3106–3095 cm^{-1})

130 ¹), and the C-H stretching regions in the 2952–2851 cm⁻¹ range are all characteristics of
131 crystalline chitin and/or a protein motif⁹. The detail bands and functional groups are assigned
132 in **SI Table 1**.

133 **Morphology of the organic fibre extracts**

134 Surface imaging of the organic fibres shows ultrastructural features of biopolymers, although
135 the fibre morphology varies from shell to shell (**Fig. 3**). Organic fibres in *L. anatina* contain
136 pores between the fibres (**Fig. 3a**), and closer imaging of the radiating units of the ridges reveals
137 organic granules (**Fig. 3a'**). The organic fibre extract from *D. tenuis* shows native lamellar
138 units (**Fig. 3b**). These are compare with the rheomorphic folding discussed by previous authors
139 ⁷, suggesting that in the present study the polymeric structure of the polysaccharide is preserved
140 ²⁶. Organic nanofiber ultrastructure typical of chitin is observed in *D. tenuis* (**Fig. 3b'**), unlike
141 the fibrous structure found in the organic fibre extract of *L. anatina*.

142 **Structural imaging of brachiopod shells after demineralization and deproteination**

143 In the shells of *Lingula*, there are apatite-rich lamellae and organophosphatic-rich lamellae
144 (**Figs. 4a, b**). The thickness of the apatite-rich layers is up to 840 nm, whereas the thickness of
145 the organophosphatic-rich lamellae is up to 1.5 μm (**Fig. 4a**). In the organophosphatic lamellae,
146 the organic sheet laminations are parallel to the Ca-phosphate sub-lamellae (**Fig. 4b**), but do
147 not permeate into the apatite-rich lamellae which are roughly perpendicular (**Fig. 4b**). Within
148 the apatite-rich laminae of *Lingula*, there are nanoscale fibrils that are mineralized with Ca-
149 phosphate nanoparticles (~ 50–70 nm) to form a fibrous biocomposite (**Fig. 4c**). FEG-SEM
150 imaging of *Lingula* reveals composite organic sheets with Ca-phosphate granules (**SI Fig. 3a**).
151 These represent several layers that were peeled off the shells to form organic fibres for this
152 study (see materials and methods). Some biomineralized nanofibrils are arranged
153 approximately perpendicular to the micro-laminations (**SI Fig. 3a**).

154 After demineralization and deproteination, the shell of *Discinisca* is permeated by canals with
155 diameters of ~90–120 nm (**Fig. 4d**). The conspicuous sets of canals consist of laminae with
156 various aggregates of organic-coated granules in the 50–100 nm range (**Fig. 4e**; **SI Fig. 3b**).
157 As shown in **Fig. 4f**, the shell of *Discinisca* is composed of ~50–60 nm spherical Ca-phosphate
158 nanoparticles, with the aggregates of protein-coated granules naturally compacted to form
159 mosaics (see **Fig. 4f**), and compare with the previous study⁷. Rod-shaped crystallites (**Fig. 4f**)
160 may perhaps be self-organized chitin fibrils, which are coated with proteins before
161 mineralization. The apatitic components entwine with the chitin-protein fibrils (**Fig. 4e**),
162 resulting in a stratiform succession of microscale laminae^{22,30}.

163 **Thermal gravimetric analysis and differential thermal gravimetric analysis**

164 TGA and DTG analysis of brachiopod shell samples and standard α -chitin was carried out to
165 detect degradation features in the organic matrix. TGA weight losses and multistage
166 decompositional steps occur for the brachiopod shells and α -chitin (**Fig. 5**). The first weight
167 loss of 5.1 wt% to 5.6 wt% for both *L. anatina* and *D. tenuis* occurs over the 30–200°C range,
168 and is attributed to removal of water. The second weight loss of 26.6 wt% for *L. anatina* and
169 12.9 wt% for *D. tenuis* (**Fig. 5a**) is recorded in the 200–650°C range and is due to the
170 combustion of a complex mixture of shell macromolecules, including chitin fibre and a protein
171 moiety^{25,31}, that is occluded in the apatitic shell biominerals. The maximum DTG value for the
172 commercially-used α -chitin is recorded at 357°C, whereas the peak shift occurs at 335°C for
173 *L. anatina* and 347°C for *D. tenuis* (**Fig. 5b**). The values for the shell biominerals are in the
174 250–350°C range for thermal stability of β -chitin^{25,31}. Lower temperature peaks are considered
175 a measure of lower thermal stability³¹. However, the DTG thermogram of *L. anatina* is similar
176 to α -chitin, and shows a broad peak at around 600°C (**Fig. 5b**), which is attributed to the thermal
177 degradation of a pyranose ring and the decomposition of residual carbon³¹. DTG thermograms
178 of shell biominerals reveal apatitic peaks at 840°C for *L. anatina* and 740°C for *D. tenuis*. The

179 residual mass after heating to 900°C is 65.9 wt% for *L. anatina* and 79.6 wt% for *D. tenuis*.
180 This suggests the presence of inorganic matrices that were not extracted during the acid-
181 treatment stage.

182 **Ultrastructural imaging of brachiopod shells**

183 The organophosphatic-shelled brachiopods were heated to remove organic layers and granules
184 in order to reveal the skeletal ultrastructure using FEG-SEM (**Figs. 6 and 7**). After complete
185 demineralization, deproteinization and thermal analyses, the brachiopod shells maintained
186 structural integrity. Back-scattered electron imaging of the external shell surface of *Lingula*
187 shell reveals a very similar ultrastructure to the original shell prior to thermal treatment (see **SI**
188 **Fig. 4**), with many features retained such as pores (canals) and Ca-phosphate rod-shaped lathes
189 (**Fig. 6a**). The diameters of the pores are between 123.6-152.1 nm long and 230.3-371.4 nm
190 wide. The shells of *Lingula* have two layers: the primary layer is ~ 20 µm thick, while the
191 secondary layer is ~8 µm thick (**Fig. 6b**). Higher magnification of the shell cross-section
192 displays the morphology of the primary layer (**Fig. 6c**), which is different from the secondary
193 layer that is made of thin, overlapping tablets (**Fig. 6d**). Each tablet in *Lingula* shells is
194 rhomboidal, with lengths up to 12.2 µm and widths up to 6.6 µm. In contrast, the primary layer
195 is organised into overlapping rod-shaped lathes that are several nm long and are of different
196 shapes, but are not deformed despite thermal gravimetric analysis.

197 The shell of *D. tenuis* is composed of a single layer that is 21 µm thick (**Fig. 7a**). Higher FEG-
198 SEM magnification of the shell cross-section shows that rod-shaped lathes are arranged in
199 alternating orientations. The rod-shaped lathes are several hundred nm long (**Fig. 7b**). The
200 external surface of *D. tenuis* is composed of rod-shaped lathes that are randomly oriented and
201 of variable size and shape, with most lengths up to 3.8 µm and widths up to 375 nm (**Fig. 7c**).
202 The large columnar crystal in **Fig 7c** is 7.2 µm long and 1.3 µm wide. FEG-SEM imaging

203 reveals spherical imprint tablets (**Fig. 7d**), with the inner component composed of rod-shaped
204 lathes (**Fig. 7e**). Interestingly, this observation contrasts to previous work which showed the
205 inner layer of a uni-lamellar tablet of *D. tenuis* was composed of small granules³². This
206 disparity could be attributed to the different growth stages of brachiopod shells: the present
207 study analysed a mature shell of *Discinisca*, while Williams et al. (2001) analysed juvenile
208 shells. In the shell's studied here, the diagonal length of the largest tablets is 19.7 μm , while
209 most tablets are $\sim 16 \mu\text{m}$ long and $\sim 15 \mu\text{m}$ wide (**Fig. 7d**).

210 **MicroRaman and energy dispersive X-ray spectroscopy of skeletal apatitic shells after** 211 **heating**

212 After thermal analysis of *L. anatina* and *D. tenuis*, Raman spectra amide bands and other
213 organic bands that were originally present (**Fig. 1**) are no longer visible (**Fig. 8a**). Instead, the
214 Raman spectra reveal the internal vibrational modes of phosphate groups (**Fig. 8b**). The strong
215 absorption band at 964 cm^{-1} is assigned to $\nu_1\text{PO}_4^{3-}$ and is due to the non-degenerated symmetric
216 stretching of the P-O band. Bending modes of two $\nu_2\text{PO}_4^{3-}$ vibrational bands appear at 430 cm^{-1}
217 and $\sim 450 \text{ cm}^{-1}$. The bands present in the $1035\text{--}1080 \text{ cm}^{-1}$ range are assigned to the triply
218 degenerated asymmetric stretching mode of $\nu_3\text{PO}_4^{3-}$. It is speculated that the specific bands at
219 1042 , 1053 and 1080 cm^{-1} correspond to typical fluorapatite^{33,34}. The vibrational mode at
220 $\sim 1022 \text{ cm}^{-1}$ is a characteristic of apatite containing divalent ions and vacancies on the crystals
221 instead of monovalent ions^{35,36}. In the region of the $\nu_4\text{PO}_4^{3-}$ bending mode, four distinguishable
222 bands appear at 581 , 591 , 607 and 617 cm^{-1} . The 997 cm^{-1} and 1010 cm^{-1} bands correspond to
223 the P-O stretching vibration of monohydrogen phosphate (HPO_4^{2-}). A 1010 cm^{-1} band occurs
224 in the octacalcium phosphate phase^{36,37}, whereas a 997 cm^{-1} band occurs in an apatitic
225 environment^{34,38}. The *D. tenuis* spectrum reveals a small 648 cm^{-1} band that corresponds to a
226 librational mode of the hydroxyl groups and/or the ν_4 in-plane deformation bending mode of
227 CO_3^{2-} ^{33,36}. The small band at 870 cm^{-1} arises from the bending mode (ν_2) of the CO_3^{2-} group³⁶

228 and/or HPO_4^{2-} ions ³⁹. The bands at 795 cm^{-1} and 828 cm^{-1} in the *L. anatina* spectrum
229 correspond to ν_4 deformation bending modes of CO_3^{2-} ³³.

230 Energy dispersive X-ray measurements after thermal gravimetric analysis reveal that calcium,
231 phosphorus, oxygen, carbon and fluorine are the dominant elements in both samples, with
232 minor magnesium (**SI Fig. 5**). In addition, minor sodium and sulphur were identified in *D.*
233 *tenuis* shell. The sulphur signal is assigned predominantly to left-over sulphated
234 glycosaminoglycans. The calcium-phosphorus atomic ratio in *L. anatina* ranges from 1.69:1
235 (primary layer) to 1.71:1 (secondary layer), similar to the ratio of *D. tenuis* (1.66:1). The
236 calcium-phosphorus atomic ratios in this study are similar to the expected ratio of 1.67:1 for
237 hydroxyapatite, $\text{Ca}_{10}(\text{PO}_4)_6(\text{OH})_2$.

238 **Discussion**

239 The presented data provide a much better characterisation of the core organic fibres in two
240 extant organophosphatic brachiopod shells that have a long fossil record, compared to previous
241 studies ⁶. The core fibres are structure-forming and stabilizing polysaccharides, composed of
242 chitin. After purification, the thermal degradation results confirm the presence of a chitin
243 matrix in the shells of two representative taxa belonging to separate superfamilies of lingulid
244 organophosphatic brachiopods, *L. anatina* (Linguloidea) and *D. tenuis* (Discinoidea). The *L.*
245 *anatina* shells are composed of two-fold more abundant chitin matrix compared to the *D. tenuis*
246 shells. Chitin is rarely found in a pure state in nature, and is most commonly linked covalently
247 with proteins ⁴⁰. Pure chitin can be difficult to isolate, for example in mollusc shell biominerals
248 ^{1,41} and brachiopod shells ⁶. Nevertheless, chitin can be readily distinguished using vibrational
249 spectroscopy, such as by Raman and FTIR spectroscopy, due to their distinctive bands ²³⁻²⁵.
250 The analyses presented here using vibrational spectroscopy reveal chitin fibres entwined with
251 minor shell proteins, supporting previous work ⁶.

252 The spectral bands of the organic fibres compare closely with the chitinous system containing
253 amino-polysaccharide chitin (**Figs. 1 and 2**). The FTIR and Raman spectra bands associated
254 with the amide I vibrational modes reveal broad and complex bands that are centred at high
255 frequencies and are attributed to β -chitin. The Raman band is centred at $\sim 1655\text{ cm}^{-1}$ for
256 brachiopod shells, and is commonly assigned to stretching of the C=O group hydrogen bonded
257 to N-H group of the neighbouring intra-sheet chain²⁴. In the FTIR spectra, the amide I position
258 is at 1652 cm^{-1} for *D. tenuis*. The band shifts by $\sim 19\pm 3\text{ cm}^{-1}$ towards a lower frequency for *L.*
259 *anatina* (**SI Table 1**). The FTIR spectra 1634 cm^{-1} band for *D. tenuis* and a 1646 cm^{-1} band for
260 *L. anatina* are present as a shoulder, and are likely due to defects in the crystalline structure of
261 the chitin fibre, or possibly a shell-associated protein. The deconvolutional fit of the amide I
262 band for FTIR spectra in the $1580\text{--}1720\text{ cm}^{-1}$ range also reveals the band at $\sim 1622\text{ cm}^{-1}$,
263 compare with the α -chitin band at 1620 cm^{-1} (**SI Fig. 6**). The occurrence of this band may show
264 a specific hydrogen bond of carbonyl (C=O) with the hydroxymethyl group of the next chitin
265 residue of the same chain or due to the presence of enol form of the amide moiety^{42,43}. A ~ 1003
266 cm^{-1} phenyl ring vibration is visible in the Raman spectra of the studied brachiopod shells,
267 and is commonly observed in the published spectra of collagen^{27,28}. Recent analyses provide
268 comprehensive data on *D. tenuis* and *L. anatina* shells, with identification of a collagen matrix
269 as the primary protein motif within the inorganic matrix of phosphate-shelled brachiopods²⁹.

270 After demineralization and deproteination, TGA reveals phosphatic soluble macromolecules
271 of 14.0 wt.% for *L. anatina* and 11.7 wt.% for *D. tenuis*. Based on the previous work of L  v  que
272 et al.⁴⁴, there may be soluble shell proteins in Ca-phosphate shell biominerals that greatly
273 contribute to the formation of crystalline apatite. The inorganic matrix provides the structural
274 strength, stiffness and rigidity for many invertebrate shell biominerals, including
275 organophosphatic brachiopod shells⁴⁵. However, polysaccharide chitin offers increased
276 strength and flexibility^{45,46}.

277 *L. anatina* is clearly laminated with an alternating chitinous system and biomineralized chitin-
278 phosphate layers. In contrast, lamination of the mineralization framework is less pronounced
279 in the sessile epibenthic *D. tenuis*^{45,46}. These authors concluded that biomineralized laminae
280 provide strength to the shells of *L. anatina*, and allow bending flexibility, a factor that may
281 have been important in the more complex shell-first burrowing of living lingulids. However,
282 flexibility is less important for the shallow marine epibenthic phosphate-shelled brachiopods
283⁴⁵. The analyses reported here reveal the spatial ultrastructure, apatitic and polysaccharide
284 matrix of two important phosphate-shelled brachiopods, and demonstrate an effective
285 bioanalytical approach for analysis of lophotrochozoan shell biominerals.

286 The FEG-SEM imaging, after thermal analyses, reveals pores and spaces that were probably
287 originally occupied by organic macromolecules and/or amorphous Ca-phosphate particles in
288 the phosphate-shelled brachiopods (**Figs. 6; 7**). Cross-sections of *L. anatina* shells show rod-
289 shaped lathes that are continuous, and rhomboidal tablets (**Fig. 6**). In contrast, cross-sections
290 of *D. tenuis* reveal small domains of rod-shaped crystals within a confined Ca-phosphate
291 mineral phase (**Fig. 7a** and **b**). In the absence of crystals, it seems that Ca-phosphate
292 confinement restricts the growth of the apatitic crystallites, consistent with the formation of
293 bone-like crystalline apatite⁴⁷. Although the external shell surface of *D. tenuis* confirmed
294 several rod-shaped crystals that are randomly orientated, these are not comparable to the crystal
295 lathes that form the external surface of *L. anatina*.

296 The SEM imaging of *D. tenuis* after thermal analysis reveals apatitic tablets, confirming the
297 previous work of Williams et al³². These authors also revealed a siliceous mosaic in the
298 metamorphosis larval shell of *D. tenuis*, whereas this study shows almost no silicon peak in the
299 EDX analysis of *D. tenuis* (**SI Fig. 5**). However, EDX after thermal analysis reveals a sulphur
300 band which is incorporated into apatitic aggregates. Williams et al³² suggested that the matrix
301 of the tablets is mainly a soluble polymer, presumably sulphated glycosaminoglycans.

302 **Conclusions**

- 303 1. Based on field emission gun scanning electron microscopy and vibrational
304 spectroscopic analyses, phosphate-shelled brachiopods (*Lingula anatina* and
305 *Discinisca tenuis*) contain chitin fibre composites with a fibrous protein concentration,
306 which create suitable microenvironments for inorganic nanoparticle aggregation.

- 307 2. The polysaccharide-apatitic matrix composition of the shells of *L. anatina* is distinctly
308 different from that of *D. tenuis*. For *L. anatina*, polysaccharide fibre component is
309 internally reinforced by nanoscale Ca-phosphate matrix and distinctively laminated. A
310 different shell design apparently favours *D. tenuis* in that it contains a continuous
311 compact layer with canals and does not contain non-mineralized laminae.

- 312 3. It is proposed that the high content of the polysaccharide chitin matrix of *L. anatina*
313 may contribute to its complex burrowing mechanism, in which the valves function as
314 flexible digging tools combined with the injection of water in the shell-first burrowing,
315 thus producing U-shaped burrows. The chitin matrix of *L. anatina* is composed of brittle
316 sheets or lamellae, forming a laminar shell design that produces a flexible shell. A
317 flexible shell gives an advantage for burrowing and prompt movements in the burrow
318 ^{10,11,16-18}.

- 319 4. This study highlights the differences in the skeletal ultrastructures of *L. anatina* and *D.*
320 *tenuis*. *L. anatina* has a distinctive two-layer structure, while *D. tenuis* has a single layer
321 with an imprint of a Ca-phosphate mineral. However, based on TGA, the amount of
322 soluble shell macromolecules is similar, 14.0 wt.% for *L. anatina* and 11.7 wt.% for *D.*
323 *tenuis*.

324 **Materials and methods**

325 **Materials**

326 Three phosphatic brachiopod shells belonging to *Lingula anatina* Lamarck, 1801 and
327 *Discinisca tenuis* Sowerby, 1847 (SI Fig. 7) were used for this study, including both recently
328 alive and live specimens (modern). Recently alive shells of *D. tenuis* and *L. anatina* were
329 collected from Walvis Bay, Namibia, and from Moreton Bay, Queensland, Australia,
330 respectively. The live specimens of *L. anatina* that were used in this study were collected in
331 the Bay of Guangxi, China, and were preserved in 10% formalin. While long exposure of
332 biological samples to formalin does not alter the organic composition, it does diminish the
333 fracture toughness due to etching/removal of calcium phosphate. Shells of brachiopods are
334 laminated and are covered with a non-mineralized organic layer, the periostracum, which
335 ranges from 1–30 μm thick^{30,48}.

336 **Sample preparation and thermal gravimetric analysis**

337 The three shell samples were mechanically cleaned with a scalpel, and then washed with Milli-
338 Q water to remove organic and inorganic contaminants. Samples were soaked in hydrogen
339 peroxide (35%; Chem-Supply, UN2014) for about 2 hours to remove surface organic detritus.
340 Each shell sample was demineralized with 5% acetic acid at room temperature for about 48 h.
341 Subsequently, shell samples were washed several times with Milli-Q water, followed by
342 deproteinisation and/or depigmentation with 5% NaOH at room temperature for 40 h. Several
343 layers were peeled off the shells using a tweezer after 24 h in NaOH, and are termed the organic
344 fibres. The remaining shell samples and the organic fibres were collected from the solution,
345 washed in Milli-Q water until a pH of about 6.8 was reached, and then rinsed in cold acetone
346 twice. The shell samples and organic fibres were then dried at room temperature.

347 Shell samples was broken into a few mm-sized pieces and was heated using a thermal
348 gravimetric analyzer (TGA) model 2050 (TA Instruments, USA) equipped with a differential
349 thermal gravimetric (DTG) analyzer. About 10 mg of sample was measured at a rate of

350 10°C/min over a temperature interval from 25°C to 900°C. The moisture content, organic
351 biopolymer content, and residual ash content were determined from mass losses. The analyses
352 were recorded twice for each sample. α -chitin extracted from shrimps (Sigma-Aldrich) was
353 used as a standard for this study.

354 **MicroRaman and Fourier transform infrared Spectroscopy**

355 Raman spectra were recorded at room temperature using a Horiba Jobin Yvon LabRAM HR
356 Evolution spectrometer equipped with an Olympus BX41 microscope and an automated x-y
357 stage. A red wavelength helium-neon laser (633 nm) was used and scattered light was dispersed
358 by a grating with 600 grooves/mm (750 nm spacing). Rayleigh radiation was blocked using an
359 edge filter. Spectra of the organic fibres were recorded in the 400–1800 cm^{-1} range with an
360 acquisition time of 60 s, 10 accumulations, and a delay time of 3 s. In contrast, spectra of the
361 minerals after TGA analyses were acquired with an acquisition time of 2–5 s, 20
362 accumulations, and time was not delayed. For each sample, 3–4 spots were measured for
363 spectral clarity. Data acquisition and spectra treatment were carried out with the commercially
364 available program LabSpec v6 (HORIBA Jobin Yvon GmbH).

365 FTIR measurements were conducted as described previously ¹, with 64 accumulations and a
366 resolution of 2 cm^{-1} . Background spectra were measured at the start of each analysis. Spectra
367 treatments were performed using the software Origin LabPro 2017. A linear baseline was
368 subtracted for the spectra and for the amide I region, over the range of 1580–1720 cm^{-1} . Peak
369 fitting of the spectra was performed to reveal the different components of a spectrum based on
370 Gaussian functions.

371 **Field emission gun scanning electron microscope imaging and energy dispersive X-ray** 372 **analysis**

373 Both organic fibres and shell samples were mounted on aluminium SEM sample holders and
374 gold coated for imaging, prior to analysis with a JEOL JSM-7100F FEG-SEM at an electron
375 energy of 10 kV and a 10 mm walking distance. For energy dispersive X-ray (EDX) analysis,
376 samples were carbon coated and were evaluated with a Phenol XL Desktop back-scattered
377 detector SEM at an electron energy of 15 kV and 7 mm walking distance. Data were processed
378 using the Pro Suite software package.

379 **References**

- 380 1. Agbaje, O. B. A., Shir, I. B., Zax, D. B., Schmidt, A. & Jacob, D. E. Biomacromolecules within
381 bivalve shells: Is chitin abundant? *Acta Biomater.* **80**, 176-187 (2018).
- 382 2. Ehrlich, H. Chitin and collagen as universal and alternative templates in biomineralization. *Int.*
383 *Geol. Rev.* **52**, 661-699 (2010).
- 384 3. Neville, A. C. *Biology of fibrous composites: development beyond the cell membrane.*
385 (Cambridge University Press, 1993).
- 386 4. Naleway, S. E., Porter, M. M., McKittrick, J. & Meyers, M. A. Structural design elements in
387 biological materials: application to bioinspiration. *Adv. Mater.* **27**, 5455-5476 (2015).
- 388 5. Weiss, I. M., Renner, C., Strigl, M. G. & Fritz, M. A simple and reliable method for the
389 determination and localization of chitin in abalone nacre. *Chem. Mater.* **14**, 3252-3259 (2002).
- 390 6. Neary, M. T. *et al.* Contrasts between organic participation in apatite biomineralization in
391 brachiopod shell and vertebrate bone identified by nuclear magnetic resonance spectroscopy.
392 *J. R. Soc., Interface* **8**, 282-288 (2011).
- 393 7. Williams, A., Cusack, M. & Buckman, J. O. Chemico-structural phylogeny of the discinoid
394 brachiopod shell. *Philos. Trans. R. Soc., B.* **353**, 2005-2038 (1998).
- 395 8. Meyers, M. A., Chen, P.-Y., Lin, A. Y.-M. & Seki, Y. Biological materials: structure and
396 mechanical properties. *Prog. Mater. Sci.* **53**, 1-206 (2008).
- 397 9. Rahman, M. A. & Halfar, J. First evidence of chitin in calcified coralline algae: new insights into
398 the calcification process of *Clathromorphum compactum*. *Sci. Rep.* **4**, 6162 (2014).
- 399 10. Emig, C. C. Ecology of inarticulated brachiopods. *Treatise on invertebrate paleontology, part*
400 *H, brachiopoda (revised)* **1**, 473-495 (1997).
- 401 11. Thayer, C. W. & Steele-Petrovic, H. M. Burrowing of the lingulid brachiopod *Glottidia*
402 *pyramidata*: its ecologic and paleoecologic significance. *Lethaia* **8**, 209-221 (1975).
- 403 12. Harper, D. A., Popov, L. E. & Holmer, L. E. Brachiopods: origin and early history. *Palaeontology*
404 **60**, 609-631 (2017).
- 405 13. Williams, A. *Treatise on invertebrate paleontology: Part H. Brachiopoda. Linguliformea,*
406 *Craniiformea, and Rhynchonelliformea (part).* Vol. 3 (Geological society of America, 2000).
- 407 14. Williams, A. *et al.* *Treatise on Invertebrate Palaeontology (Part H, Brachiopoda Revised).* Volume 6:
408 *Supplement* (Boulder, CO, 2007).
- 409 15. Veizer, J. *et al.* $^{87}\text{Sr}/^{86}\text{Sr}$, $\delta^{13}\text{C}$ and $\delta^{18}\text{O}$ evolution of Phanerozoic seawater. *Chem. Geol.* **161**,
410 59-88 (1999).
- 411 16. Zhang, Z., Shu, D., Han, J. & Liu, J. Morpho-anatomical differences of the Early Cambrian
412 Chengjiang and Recent lingulids and their implications. *Acta Zool.* **86**, 277-288 (2005).
- 413 17. Savazzi, E. Burrowing in the inarticulate brachiopod *Lingula anatina*. *Palaeogeogr.*
414 *Palaeoclimatol. Palaeoecol.* **85**, 101-106 (1991).

- 415 18. Savazzi, E. Burrowing sculptures and life habits in Paleozoic lingulacean brachiopods.
416 *Paleobiology* 46-63 (1986).
- 417 19. Murdock, D. J. The 'biomineralization toolkit' and the origin of animal skeletons. *Biol. Rev.*
418 (2020).
- 419 20. Iwata, K. Ultrastructure and mineralization of the shell of *Lingula unguis* Linne, (Inarticulate
420 Brachiopod). *Geol. Mineral. J.* **20**, 35-65 (1981).
- 421 21. Jope, M. The protein of brachiopod shell—VI. C-terminal end groups and sodium
422 dodecylsulphate-polyacrylamide gel electrophoresis: Molecular constitution and structure of
423 the protein. *Comp. Biochem. Physiol., Part B: Biochem. Mol. Biol.* **63**, 163-173 (1979).
- 424 22. Williams, A., Cusack, M. & MacKay, S. Collagenous chitinophosphatic shell of the brachiopod
425 *Lingula*. *Philos. Trans. R. Soc., B.* **346**, 223-266 (1994).
- 426 23. Ehrlich, H. *et al.* First evidence of chitin as a component of the skeletal fibers of marine
427 sponges. Part I. Verongidae (Demospongia: Porifera). *Journal of Experimental Zoology Part B:*
428 *Molecular and Developmental Evolution* **308**, 347-356 (2007).
- 429 24. Focher, B., Naggi, A., Torri, G., Cosani, A. & Terbojevich, M. Structural differences between
430 chitin polymorphs and their precipitates from solutions—evidence from CP-MAS 13C-NMR,
431 FT-IR and FT-Raman spectroscopy. *Carbohydr. Polym.* **17**, 97-102 (1992).
- 432 25. Kaya, M. *et al.* On chemistry of γ -chitin. *Carbohydr. Polym.* **176**, 177-186 (2017).
- 433 26. Lavall, R. L., Assis, O. B. & Campana-Filho, S. P. β -Chitin from the pens of *Loligo* sp.: Extraction
434 and characterization. *Bioresour. Technol.* **98**, 2465-2472 (2007).
- 435 27. Morris, M. D. & Mandair, G. S. Raman assessment of bone quality. *Clin. Orthop. Relat. Res.*
436 **469**, 2160-2169 (2011).
- 437 28. Wopenka, B., Kent, A., Pasteris, J. D., Yoon, Y. & Thomopoulos, S. The tendon-to-bone
438 transition of the rotator cuff: a preliminary Raman spectroscopic study documenting the
439 gradual mineralization across the insertion in rat tissue samples. *Appl. Spectrosc.* **62**, 1285-
440 1294 (2008).
- 441 29. Agbaje, O. B., George, S. C., Zhang, Z., Brock, G. A. & Holmer, L. E. Characterization of
442 organophosphatic brachiopod shells: spectroscopic assessment of collagen matrix and
443 biomineral components. *RSC Adv.* **10**, 38456-38467 (2020).
- 444 30. Williams, A. & Cusack, M. Evolution of a rhythmic lamination in the organophosphatic shells
445 of brachiopods. *J. Struct. Biol.* **126**, 227-240 (1999).
- 446 31. Hassainia, A., Satha, H. & Boufi, S. Chitin from *Agaricus bisporus*: Extraction and
447 characterization. *Int. J. Biol. Macromol.* **117**, 1334-1342 (2018).
- 448 32. Williams, A., Lüter, C. & Cusack, M. The nature of siliceous mosaics forming the first shell of
449 the brachiopod *Discinisca*. *J. Struct. Biol.* **134**, 25-34 (2001).
- 450 33. Antonakos, A., Liarokapis, E. & Leventouri, T. Micro-Raman and FTIR studies of synthetic and
451 natural apatites. *Biomaterials* **28**, 3043-3054 (2007).
- 452 34. Litasov, K. D. & Podgornykh, N. M. Raman spectroscopy of various phosphate minerals and
453 occurrence of tuite in the Elga IIE iron meteorite. *J. Raman Spectrosc.* **48**, 1518-1527 (2017).
- 454 35. Penel, G., Leroy, G., Rey, C. & Bres, E. MicroRaman spectral study of the PO₄ and CO₃
455 vibrational modes in synthetic and biological apatites. *Calcif. Tissue Int.* **63**, 475-481 (1998).
- 456 36. Koutsopoulos, S. Synthesis and characterization of hydroxyapatite crystals: a review study on
457 the analytical methods. *J. Biomed. Mater. Res., Part A.* **62**, 600-612 (2002).
- 458 37. Crane, N. J., Popescu, V., Morris, M. D., Steenhuis, P. & Ignelzi Jr, M. A. Raman spectroscopic
459 evidence for octacalcium phosphate and other transient mineral species deposited during
460 intramembranous mineralization. *Bone* **39**, 434-442 (2006).
- 461 38. Rey, C., Shimizu, M., Collins, B. & Glimcher, M. Resolution-enhanced fourier transform infrared
462 spectroscopy study of the environment of phosphate ions in the early deposits of a solid phase
463 of calcium phosphate in bone and enamel and their evolution with age. 2: Investigations in
464 the ν_3 PO₄ domain. *Calcif. Tissue Int.* **49**, 383-388 (1991).

- 465 39. Ciobanu, C. S. *et al.* Synthesis, structure, and luminescent properties of europium-doped
466 hydroxyapatite nanocrystalline powders. *Journal of Nanomaterials* **2012** (2012).
467 40. Kurita, K. Chitin and chitosan: functional biopolymers from marine crustaceans. *Marine*
468 *Biotechnol.* **8**, 203 (2006).
469 41. Osuna-Mascaró, A. J., Cruz-Bustos, T., Marin, F. & Checa, A. G. Ultrastructure of the
470 interlamellar membranes of the nacre of the bivalve *Pteria hirundo*, determined by
471 immunolabelling. *PLoS one* **10** (2015).
472 42. Kumirska, J. *et al.* Application of spectroscopic methods for structural analysis of chitin and
473 chitosan. *Marine Drugs* **8**, 1567-1636 (2010).
474 43. Rinaudo, M. Chitin and chitosan: properties and applications. *Prog. Polym. Sci.* **31**, 603-632
475 (2006).
476 44. Lévêque, I., Cusack, M., Davis, S. A. & Mann, S. Promotion of Fluorapatite Crystallization by
477 Soluble-Matrix Proteins from *Lingula Anatina* Shells. *Angew. Chem. Int. Ed.* **43**, 885-888 (2004).
478 45. Merkel, C. *et al.* Mechanical properties of modern calcite-(*Mergerlia truncata*) and phosphate-
479 shelled brachiopods (*Discradisca stella* and *Lingula anatina*) determined by nanoindentation.
480 *J. Struct. Biol.* **168**, 396-408 (2009).
481 46. Schmahl, W. W. *et al.* Hierarchical fibre composite structure and micromechanical properties
482 of phosphatic and calcitic brachiopod shell biomaterials—an overview **72**(2), 541-562 (2008).
483 47. Lotsari, A., Rajasekharan, A. K., Halvarsson, M. & Andersson, M. Transformation of amorphous
484 calcium phosphate to bone-like apatite. *Nat. Commun.* **9**, 1-11 (2018).
485 48. Merkel, C. *et al.* Micromechanical properties and structural characterization of modern
486 inarticulated brachiopod shells. *J. Geophys. Res.: Biogeosci.* **112** G02008 (2007).

487

488 **Acknowledgements**

489 OBAA is grateful to Uppsala University for support through the VR Project number 2018-
490 03390. The research for this paper was supported by the Swedish Research Council (VR Project
491 no. 2018-03390 to LEH, GAB and SCG), by the National Natural Science Foundation of China
492 (41720104002, 41621003 and 41890844 to NWU members) and by a Zhongjian Yang
493 Scholarship to LEH from the Department of Geology, Northwest University, Xi'an. GAB's
494 research is also funded by a 1000 Talent Shaanxi Province Fellowship at Northwest University,
495 Xi'an.

496 **Author contributions**

497 OBAA designed the study, carried out the analyses, interpreted the data and prepare the original
498 manuscript. LY and ZZ provided live specimens of *Lingula anatina*; LEH provided recently
499 alive *Discinisca tenuis* shells and GAB gave recently alive *Lingula anatina* shells. LEH, GAB

500 and SCG coordinated the study. All authors reviewed the manuscript and gave final approval
501 for publication.

502 **Additional Information**

503 Supplementary information accompanies this paper at <https://doi.org/>

504 **Competing interests**

505 The authors declare no competing interests.

506

507 **Fig. 1** Raman spectra (acquired using a 633-nm laser) of chitin fibre from brachiopod shells:
508 *Lingula anatina* (modern/living (ML) and Recent (RL), Recent *Discinisca tenuis* (DT), and
509 pure α -chitin (Ch) as a reference. The baselines of the spectra are corrected. The amide I single
510 band at $\sim 1654\text{ cm}^{-1}$ is due to chitin fibre, and is characteristic of β -chitin. This is dissimilar
511 from α -chitin that possesses double bands at 1617 and 1654 cm^{-1} . The amide I band of
512 *Discinisca* is broad compared to the *Lingula* shells. See **SI Fig. 1** for band deconvolution.
513 *Discinisca* also contains prominent phosphate (νPO_4^{3-}) vibrational modes at 964 cm^{-1} , 608 cm^{-1}
514 and 581 cm^{-1} . See **SI Table 1** for band assignments.

515

516 **Fig. 2** FTIR spectra of chitin fibre from brachiopod shells: *Lingula anatina*, Recent (RL) and
517 modern/living (ML), Recent *Discinisca tenuis* (DT), and pure α -chitin (Ch) as a reference. (a)
518 Shows a larger wavenumber range ($4000\text{--}600\text{ cm}^{-1}$) than the expanded range ($1800\text{--}600\text{ cm}^{-1}$)
519 in (b).

520

521 **Fig. 3** Field emission gun scanning electron microscope images of β -chitin organic fibre from
522 brachiopod shells. (a) Representative fibre surface of *Lingula anatina* showing pores and
523 radiating units of the ridges. (a') The ridge is expanded to show nanoparticle granules. (b, b')
524 External surface of *Discinisca tenuis* organic fibre showing a lamellar ultrastructure.

525

526 **Fig. 4** Field emission gun scanning electron microscope images of sodium hydroxide-treated
527 *Lingula anatina* (a-c) and *Discinisca tenuis* (d-f) shells. (a) Fracture surface of *Lingula* shell
528 showing apatite-rich (Ap-rich) and organophosphatic-rich (OrgPhos-rich) laminae. (b) Organic
529 sheets/fibres (blue arrows) in the organophosphatic-rich layer are highlighted. These sheets are
530 arranged roughly perpendicular to the apatite-rich layer, but do not permeate into it. (c)
531 Biomineralized ruptured fibrils (green arrows) on the fracture surface of an apatite-rich layer.
532 The nanoparticle granule sizes are in the $\sim 50\text{--}70\text{ nm}$ range. (d) Ultrastructure of *Discinisca*
533 shell depicting canals. (e) Nanoparticle granules in the $\sim 50\text{--}100\text{ nm}$ range, and organic fibrils

534 (white arrows). (f) Fracture section showing nano-rods (dashed arrows), mosaics (mc), and
535 spherical micro-apatite in the 50–60 nm range (arrowheads).

536

537 **Fig. 5** (a) Thermal gravimetric analysis data and (b) differential thermal gravimetric analysis
538 data of shell biominerals (LA: *Lingula anatina*, DT: *Discinisca tenuis*) and pure α -chitin (Ch).
539 The bar chart in (a) represents the calculated total polysaccharide chitin contents in the 200–
540 650°C range. *L. anatina* and *D. tenuis* comprise 26.6 wt.% and 12.9 wt.% total polysaccharide
541 matrix, respectively.

542

543 **Fig. 6** *Lingula anatina* shell architecture after thermal analysis by back-scattered electron
544 imaging (a) and field emission gun scanning electron microscopy (b-d). (a) Representative
545 external shell surface showing nano-sized crystal rods and well-arranged pores. (b) Image
546 highlighting the primary layer (c) that is ~20 μm thick and the secondary layer (d) that is ~8
547 μm thick. (c) Spatial imaging of the primary layer depicting overlapping rod-shaped lathes. (d)
548 Spatial imaging of the secondary layer revealing stacked rhomboidal tablets with pores. The
549 tablets are up to 12.2 μm long and 6.6 μm wide.

550

551 **Fig. 7** Field emission gun scanning electron microscope images of skeletal imaging of
552 *Discinisca tenuis* shell after thermal analysis. (a) Spatial ultrastructural architecture showing a
553 cast of the imprint pattern of a calcium phosphate mineral, the thickness of which is 21 μm . (b)
554 Detail of the shell cross-sectional image showing a domain of rod-shaped crystals within a
555 confined part of a calcium phosphate mineral. (c) External shell surface depicting the randomly
556 oriented rod-shaped crystals. (d) Image showing spherical tablets that are ~15.9 μm long and
557 ~14.8 μm wide. (e) Inset in (d) shows rod-shaped crystals in the tablets.

558

559 **Fig. 8** Raman spectra of brachiopod shells (*Lingula anatina* and *Discinisca tenuis*) after
560 thermal gravimetric analysis. (a) Complete range (400–1800 cm^{-1}) showing a large Raman
561 shift. (b) Expanded range (400–1200 cm^{-1}). See **Table 1** for band assignments.

562

563

564

565

566

567

568

569

570

571 **Table 1.** Raman band and assignment for apatitic shell biominerals after thermal gravimetric
 572 analysis.

<i>L. anatina</i>	<i>D. tenuis</i>	Assignment
430(s)	431(s)	ν_2 doubly degenerate bending modes of PO_4^{3-}
445(m)	449(m),	ν_2 doubly degenerate bending modes of PO_4^{3-}
450(sh)	455(sh)	ν_2 doubly degenerate bending modes of PO_4^{3-}
581(m)	582(sh)	ν_4 triply degenerate bending modes of PO_4^{3-}
591 (s)	591(s)	ν_4 triply degenerate bending modes of PO_4^{3-}
607(m)	607(m)	ν_4 triply degenerate bending modes of PO_4^{3-}
616(w)	617(sh)	ν_4 triply degenerate bending modes of PO_4^{3-}
637(vw)	631(vw)	ν_L librational mode of OH bond
	648 (vw)	ν_L librational mode of OH bond
795 (vw)		ν_4 in-plane deformation bending modes of CO_3^{2-}
828 (w)		ν_4 mode of CO_3^{2-} and/or PO_4^{3-} impurities
	870 (vw)	ν_2 bending mode of CO_3^{2-} group
950 (sh)		ν_1 nondegenerate symmetric stretching mode of the PO_4^{3-}
965(vs)	965(vs)	ν_1 nondegenerate symmetric stretching mode of the PO_4^{3-}
996 (w)	997(w)	ν_1 asymmetric stretching of the HPO_4^{2-}
1010(w)	1010(w)	ν_1 asymmetric stretching mode of the HPO_4^{2-}
1022(sh)	1024(sh)	ν_3 asymmetric stretching of PO_4^{3-} and/or CO_3^{2-} and crystal imperfections in nonstoichiometric apatite
1034(w)	1034(sh)	ν_3 triply degenerated asymmetric stretching mode of the PO_4^{3-}
1042(m)	1042(w)	ν_3 triply degenerated asymmetric stretching mode of the PO_4^{3-}
1053(s)	1053(s)	ν_3 triply degenerated asymmetric stretching mode of the PO_4^{3-}
1059(sh)	1063(sh)	ν_3 triply degenerated asymmetric stretching mode of the PO_4^{3-}
1080(m)	1080(m)	ν_3 triply degenerated asymmetric stretching mode of the PO_4^{3-} and/or ν_1 symmetric stretching mode of CO_3^{2-}
	1131 (vw)	ν_3 asymmetric stretching of the HPO_4^{2-} and/or ν_1 symmetric stretching mode of CO_3^{2-}
	1152 (vw)	ν_1 symmetric stretching mode of CO_3^{2-}

573 w: weak, vw: very weak; m: medium, s: strong, vs: very strong; sh: shoulder.

574

Figures

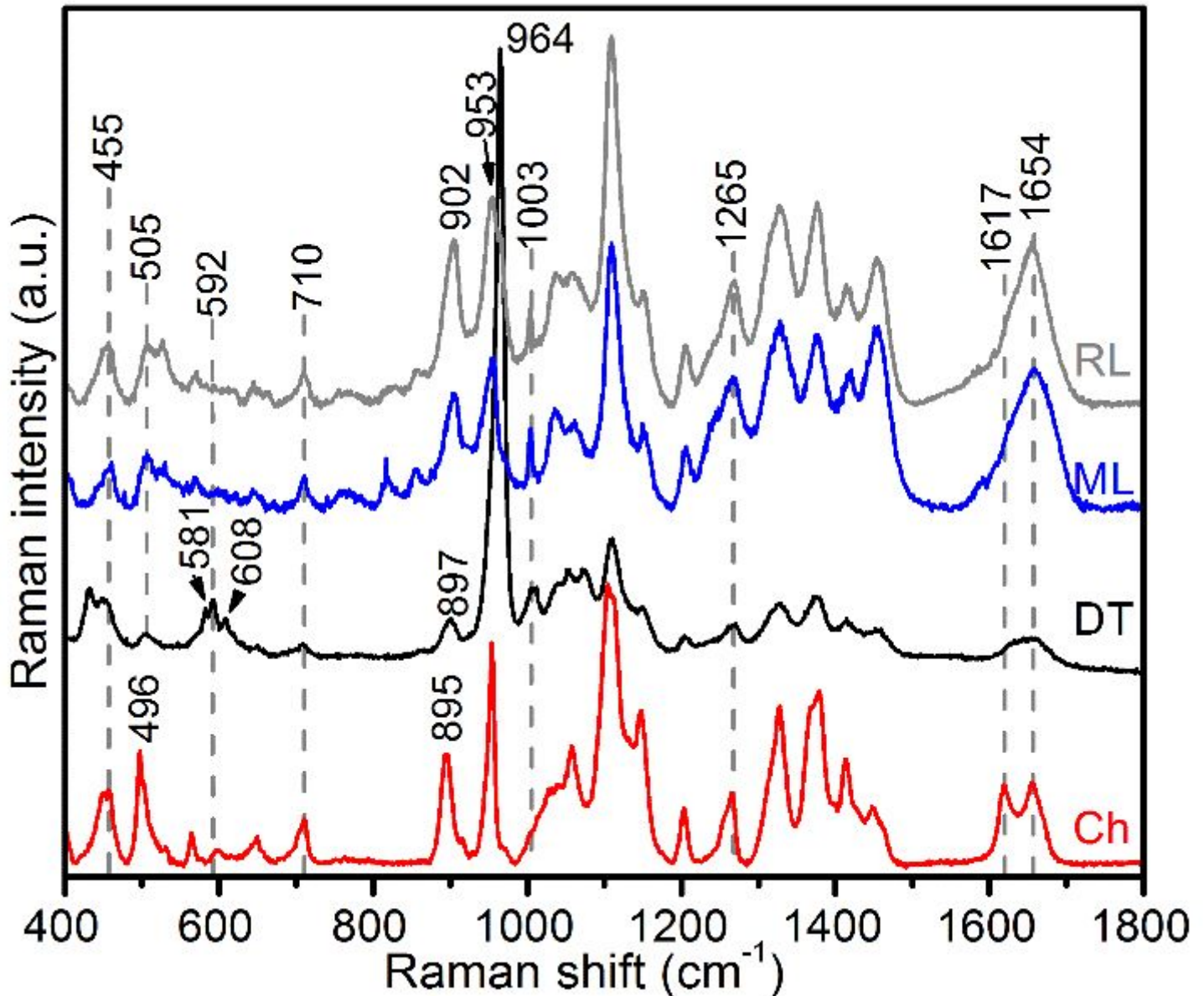


Figure 1

Raman spectra (acquired using a 633-nm laser) of chitin fibre from brachiopod shells: *Lingula anatina* (modern/living (ML) and Recent (RL)), Recent *Discinisca tenuis* (DT), and pure α -chitin (Ch) as a reference. The baselines of the spectra are corrected. The amide I single band at ~ 1654 cm⁻¹ is due to chitin fibre, and is characteristic of β -chitin. This is dissimilar from α -chitin that possesses double bands at 1617 and 1654 cm⁻¹. The amide I band of *Discinisca* is broad compared to the *Lingula* shells. See SI Fig. 1 for band deconvolution. *Discinisca* also contains prominent phosphate (ν PO₄³⁻) vibrational modes at 964 cm⁻¹, 608 cm⁻¹ and 581 cm⁻¹. See SI Table 1 for band assignments.

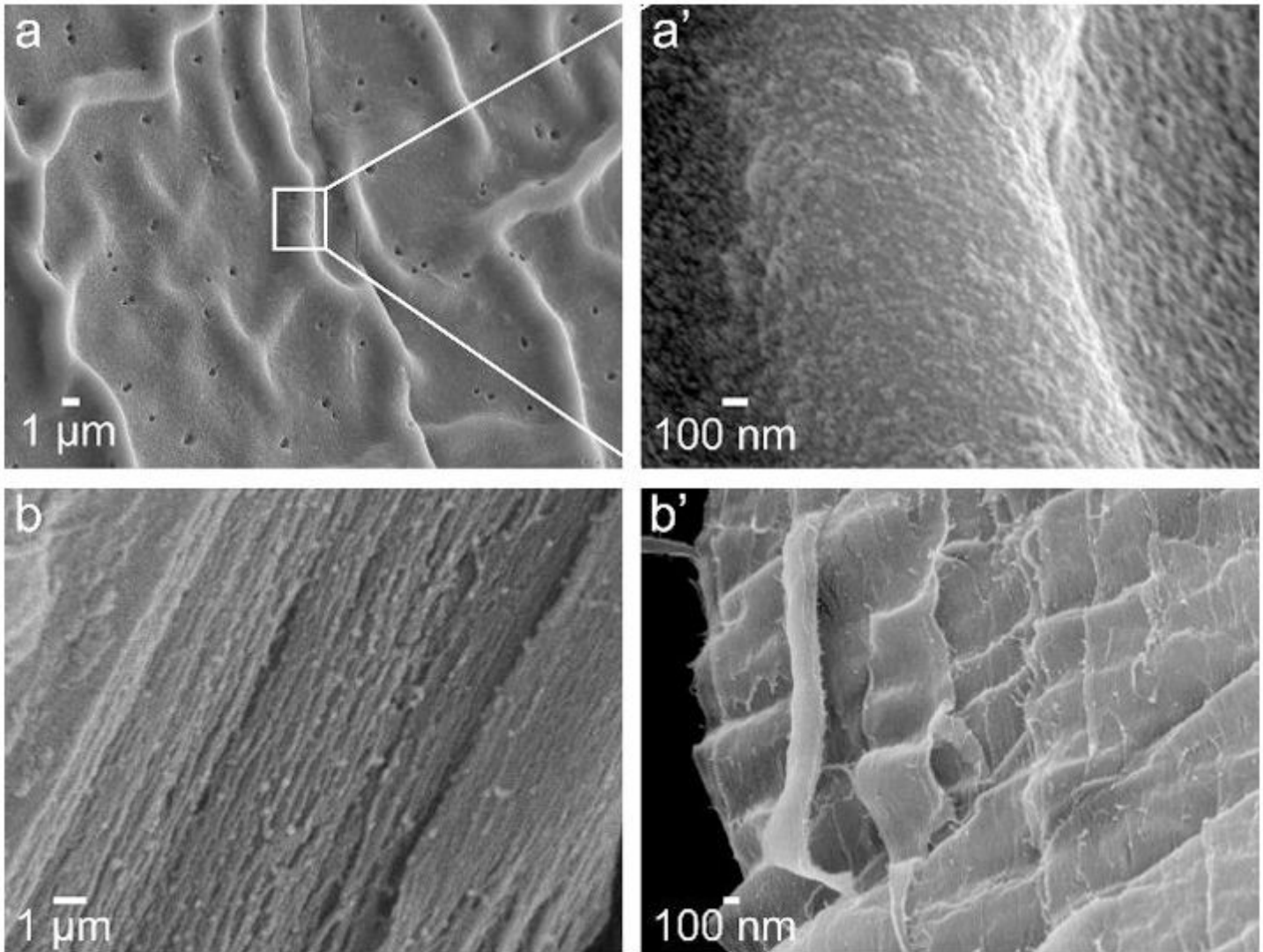


Figure 1

Field emission gun scanning electron microscope images of β -chitin organic fibre from brachiopod shells. (a) Representative fibre surface of *Lingula anatina* showing pores and radiating units of the ridges. (a') The ridge is expanded to show nanoparticle granules. (b, b') External surface of *Discinisca tenuis* organic fibre showing a lamellar ultrastructure. Note: The designations employed and the presentation of the material on this map do not imply the expression of any opinion whatsoever on the part of Research Square concerning the legal status of any country, territory, city or area or of its authorities, or concerning the delimitation of its frontiers or boundaries. This map has been provided by the authors.

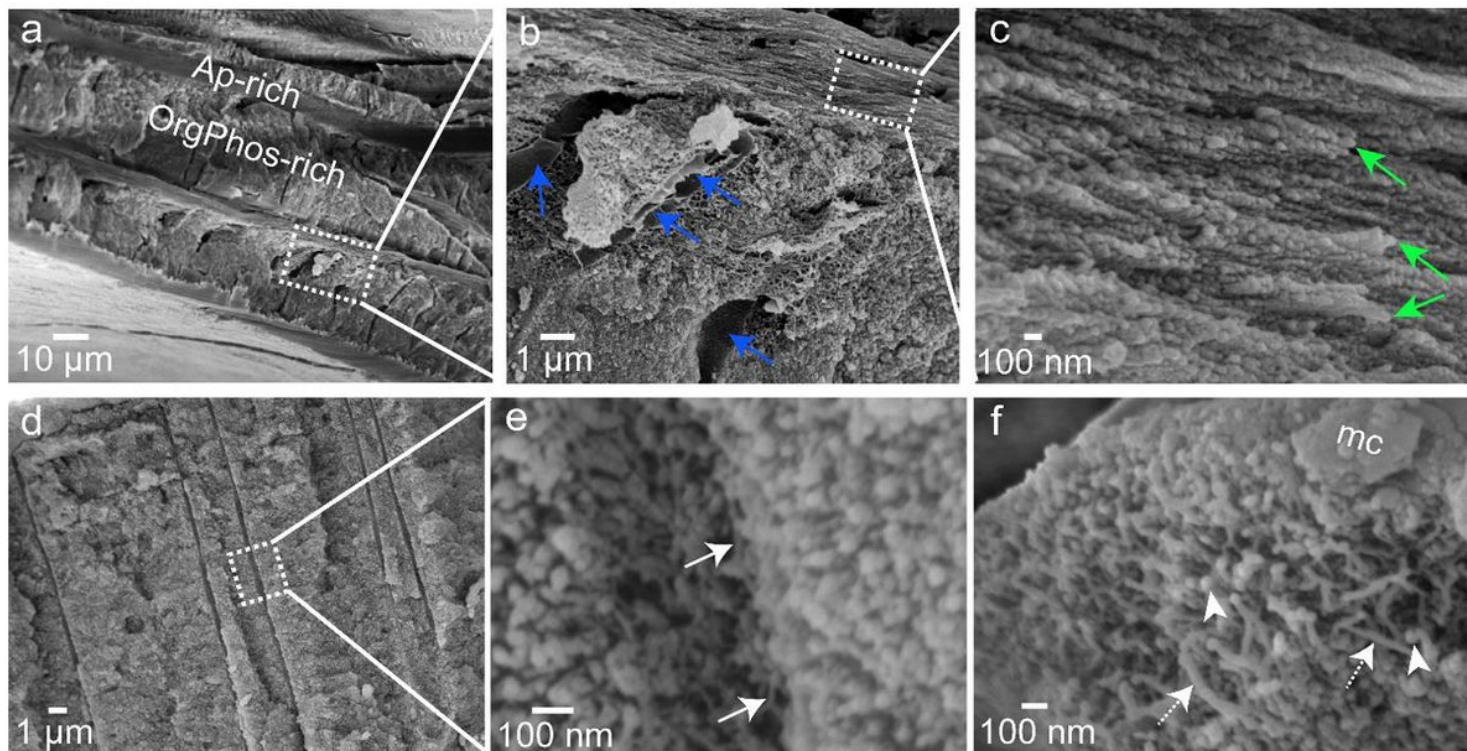


Figure 1

Field emission gun scanning electron microscope images of sodium hydroxide-treated *Lingula anatina* (a-c) and *Discinisca tenuis* (d-f) shells. (a) Fracture surface of *Lingula* shell showing apatite-rich (Ap-rich) and organophosphatic-rich (OrgPhos-rich) laminae. (b) Organic sheets/fibres (blue arrows) in the organophosphatic-rich layer are highlighted. These sheets are arranged roughly perpendicular to the apatite-rich layer, but do not permeate into it. (c) Biomineralized ruptured fibrils (green arrows) on the fracture surface of an apatite-rich layer. The nanoparticle granule sizes are in the ~50–70 nm range. (d) Ultrastructure of *Discinisca* shell depicting canals. (e) Nanoparticle granules in the ~50–100 nm range, and organic fibrils (white arrows). (f) Fracture section showing nano-rods (dashed arrows), mosaics (mc), and spherical micro-apatite in the 50–60 nm range (arrowheads). Note: The designations employed and the presentation of the material on this map do not imply the expression of any opinion whatsoever on the part of Research Square concerning the legal status of any country, territory, city or area or of its authorities, or concerning the delimitation of its frontiers or boundaries. This map has been provided by the authors.

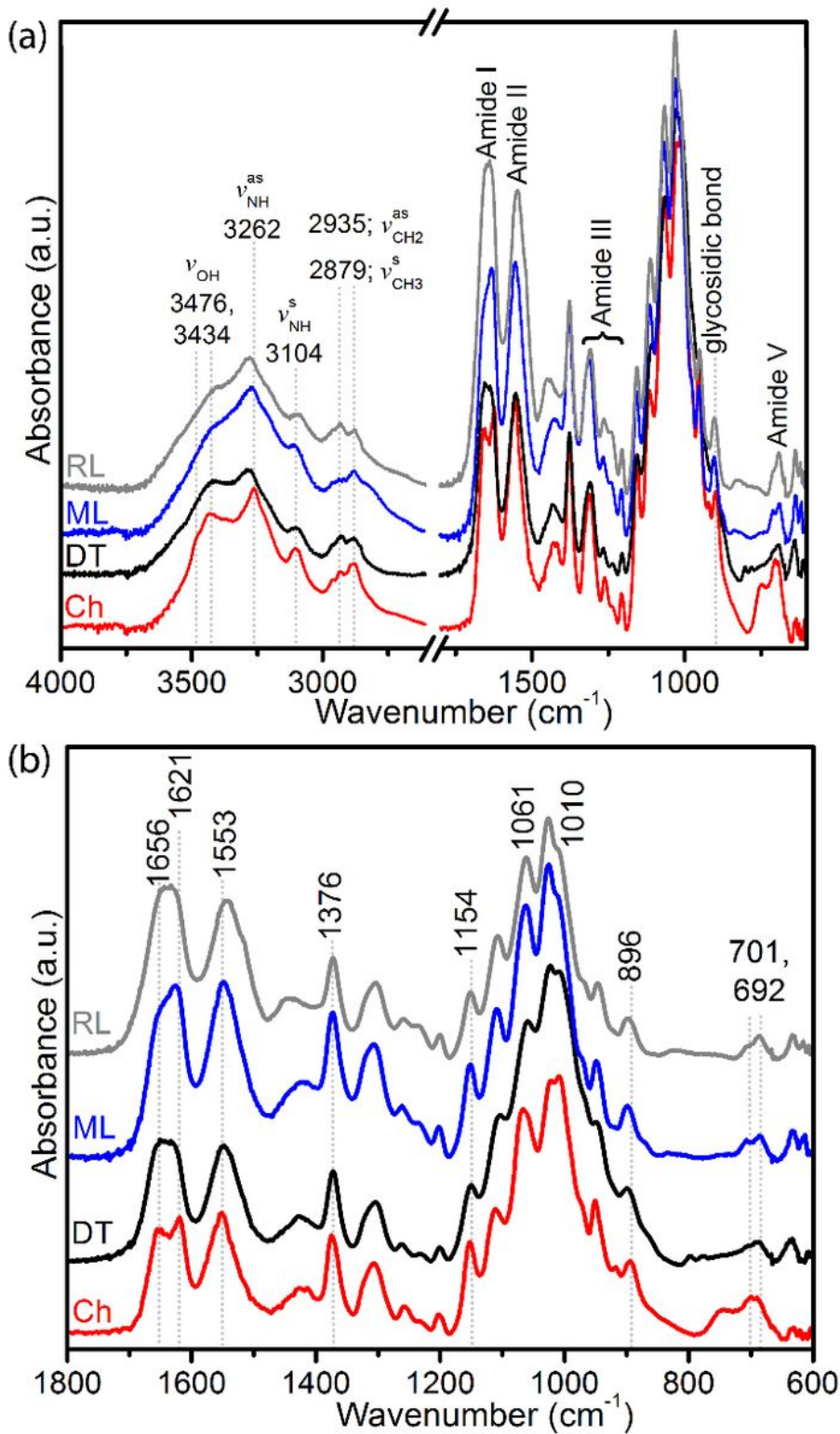


Figure 1

FTIR spectra of chitin fibre from brachiopod shells: *Lingula anatina*, Recent (RL) and modern/living (ML), Recent *Disciniscia tenuis* (DT), and pure α -chitin (Ch) as a reference. (a) Shows a larger wavenumber range (4000–600 cm⁻¹) than the expanded range (1800–600 cm⁻¹) in (b).

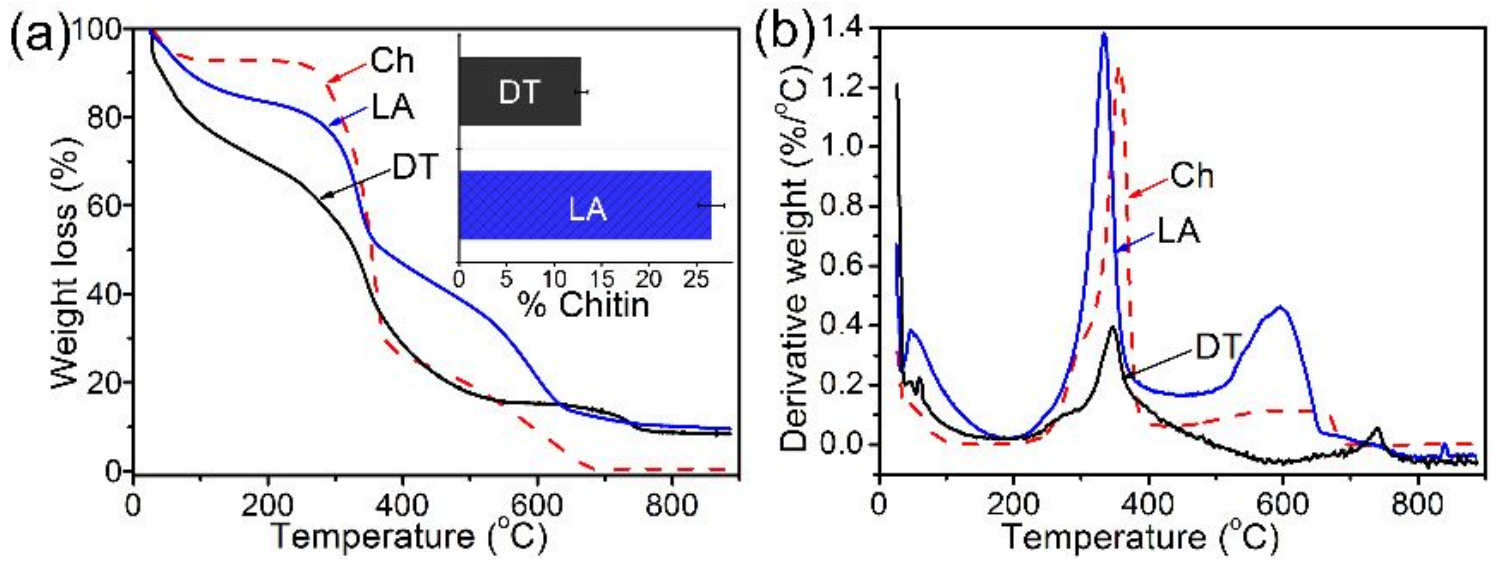


Figure 1

(a) Thermal gravimetric analysis data and (b) differential thermal gravimetric analysis data of shell biominerals (LA: *Lingula anatina*, DT: *Discinisca tenuis*) and pure α -chitin (Ch). The bar chart in (a) represents the calculated total polysaccharide chitin contents in the 200–650 $^{\circ}\text{C}$ range. *L. anatina* and *D. tenuis* comprise 26.6 wt.% and 12.9 wt.% total polysaccharide matrix, respectively.

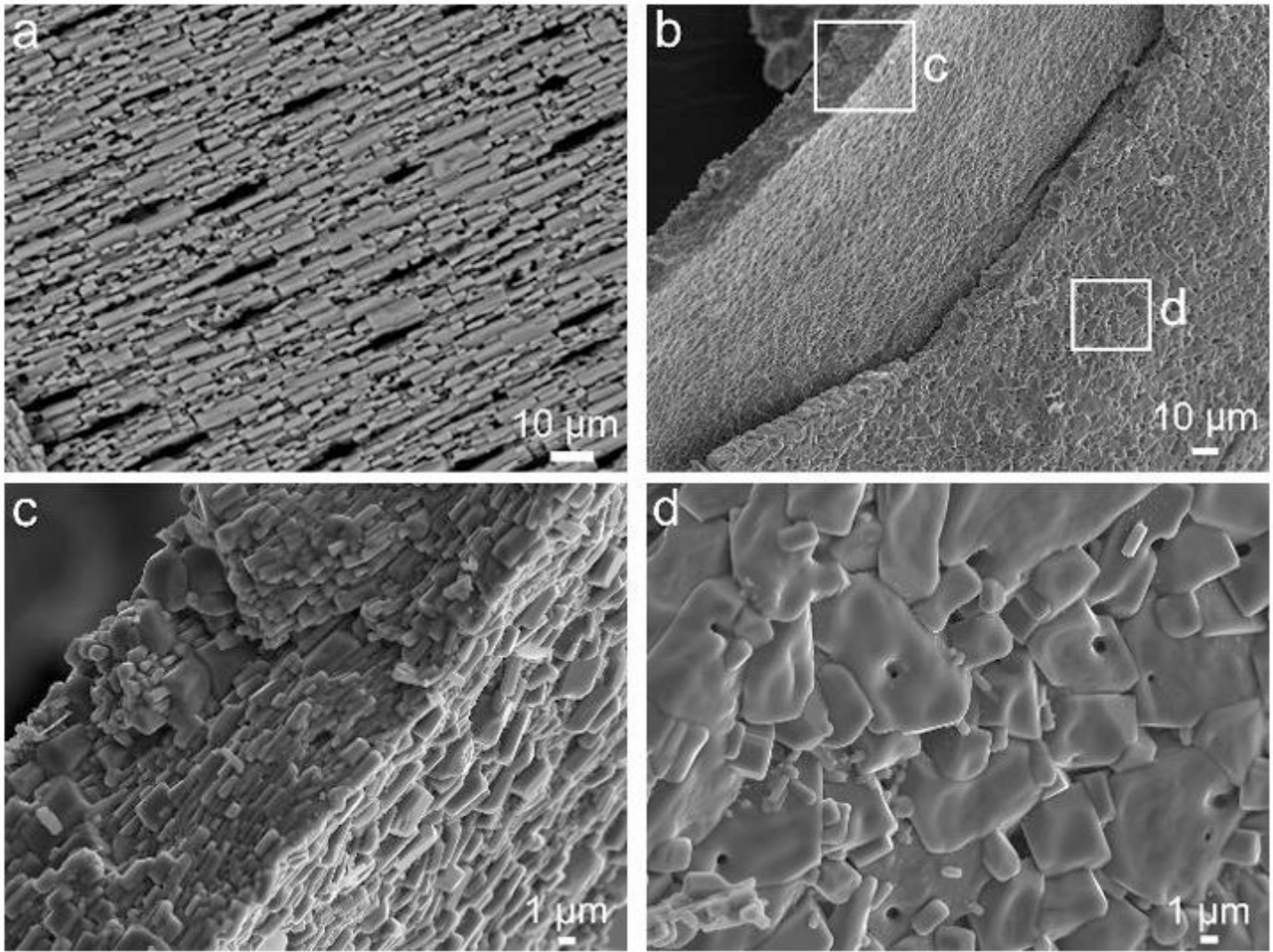


Figure 1

Lingula anatina shell architecture after thermal analysis by back-scattered electron imaging (a) and field emission gun scanning electron microscopy (b-d). (a) Representative external shell surface showing nano-sized crystal rods and well-arranged pores. (b) Image highlighting the primary layer (c) that is ~ 20 μm thick and the secondary layer (d) that is ~ 8 μm thick. (c) Spatial imaging of the primary layer depicting overlapping rod-shaped lathes. (d) Spatial imaging of the secondary layer revealing stacked rhomboidal tablets with pores. The tablets are up to 12.2 μm long and 6.6 μm wide. Note: The designations employed and the presentation of the material on this map do not imply the expression of any opinion whatsoever on the part of Research Square concerning the legal status of any country, territory, city or area or of its authorities, or concerning the delimitation of its frontiers or boundaries. This map has been provided by the authors.

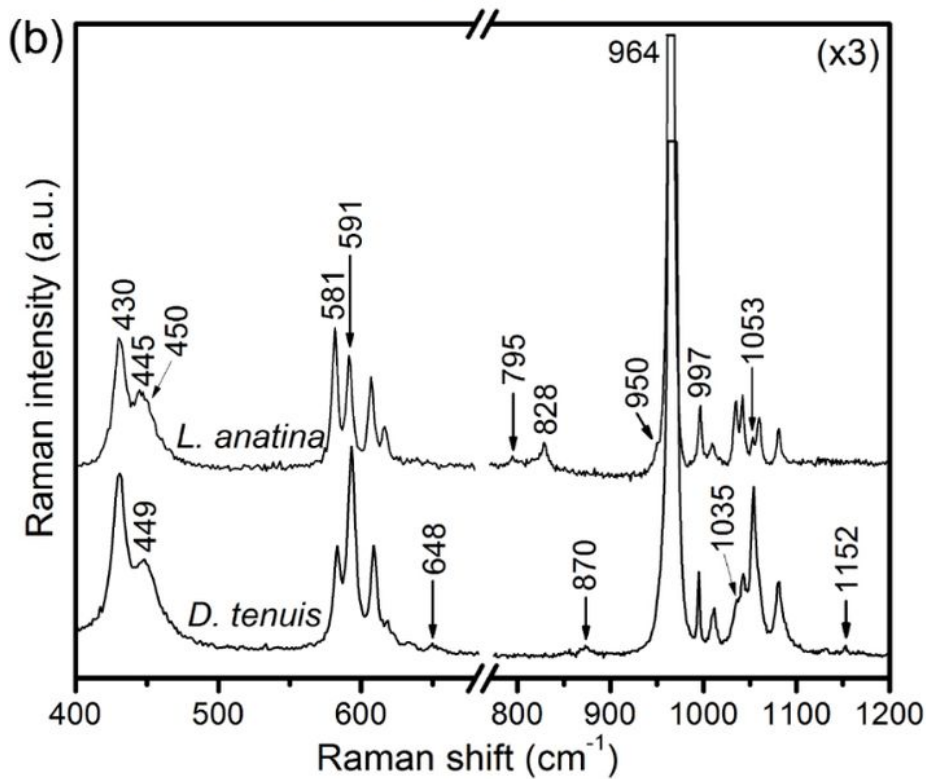
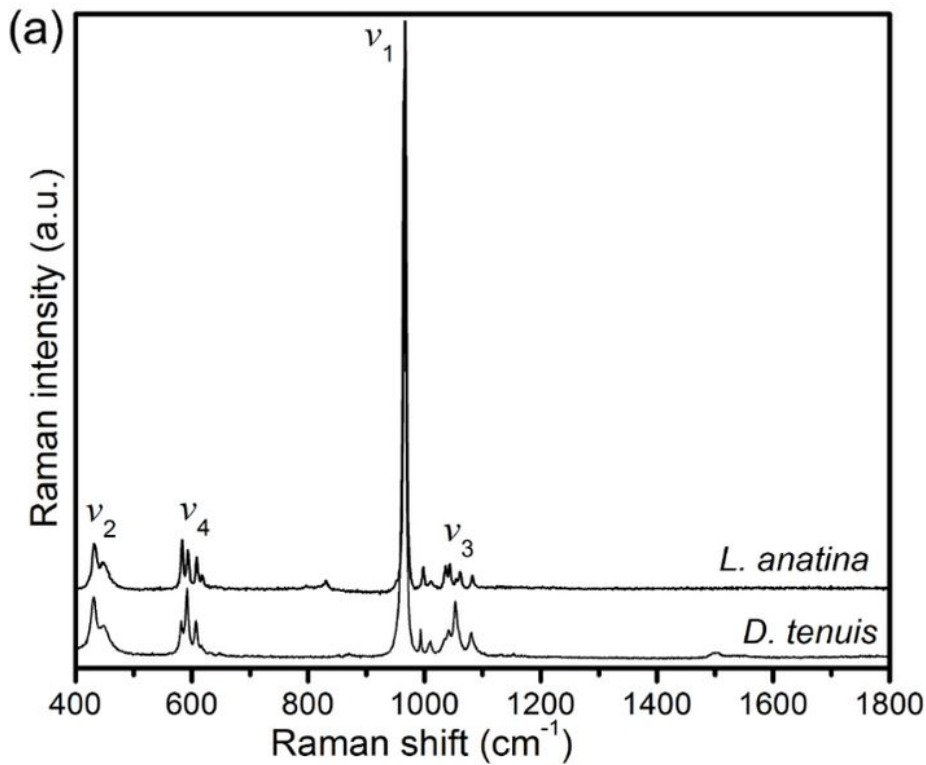


Figure 1

Raman spectra of brachiopod shells (*Lingula anatina* and *Discinisca tenuis*) after thermal gravimetric analysis. (a) Complete range (400–1800 cm⁻¹) showing a large Raman shift. (b) Expanded range (400–1200 cm⁻¹). See Table 1 for band assignments.

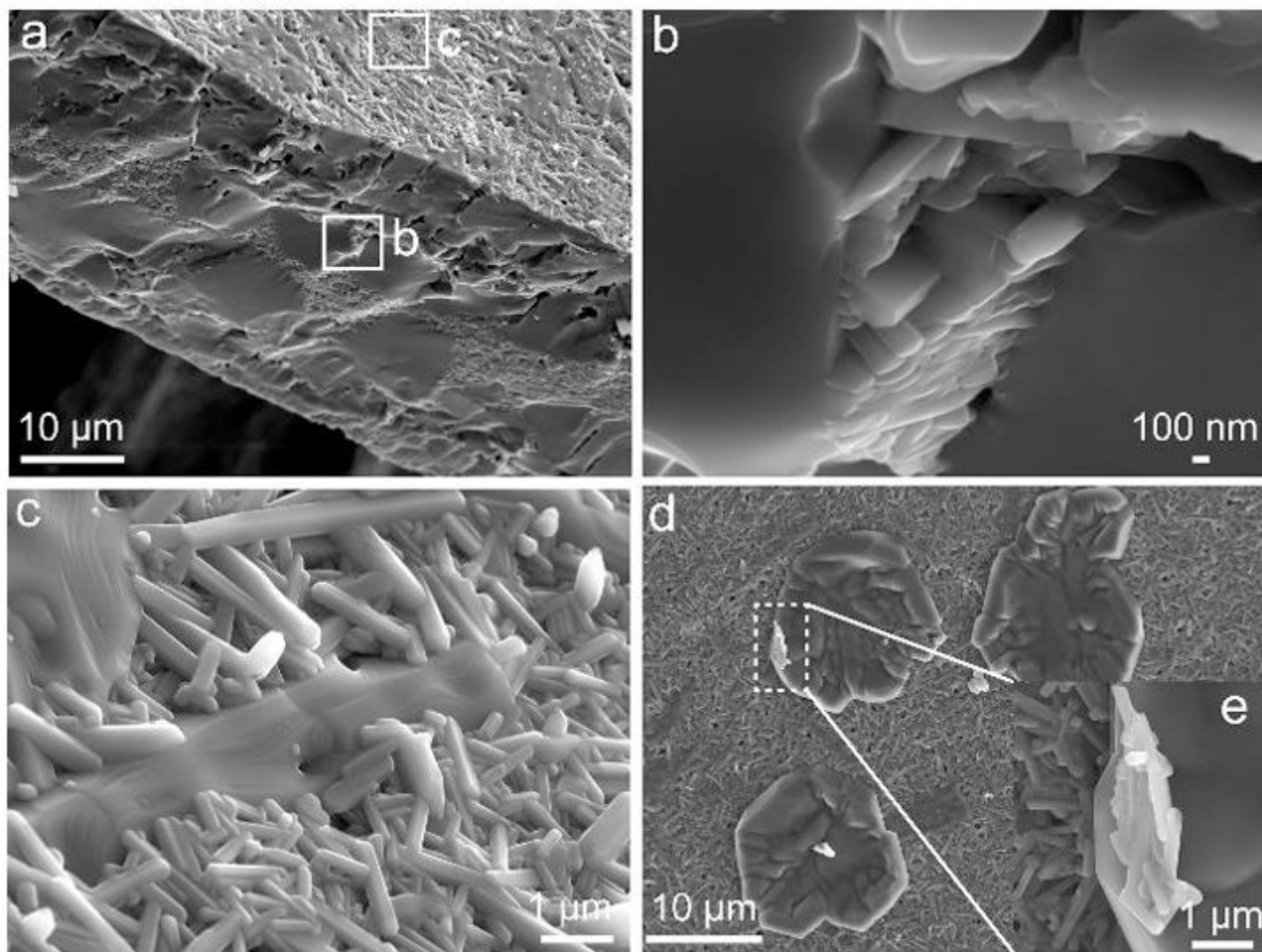


Figure 1

Field emission gun scanning electron microscope images of skeletal imaging of *Discinisca tenuis* shell after thermal analysis. (a) Spatial ultrastructural architecture showing a cast of the imprint pattern of a calcium phosphate mineral, the thickness of which is 21 μm. (b) Detail of the shell cross-sectional image showing a domain of rod-shaped crystals within a confined part of a calcium phosphate mineral. (c) External shell surface depicting the randomly oriented rod-shaped crystals. (d) Image showing spherical tablets that are ~15.9 μm long and ~14.8 μm wide. (e) Inset in (d) shows rod-shaped crystals in the tablets. Note: The designations employed and the presentation of the material on this map do not imply the expression of any opinion whatsoever on the part of Research Square concerning the legal status of any country, territory, city or area or of its authorities, or concerning the delimitation of its frontiers or boundaries. This map has been provided by the authors.

Supplementary Files

This is a list of supplementary files associated with this preprint. [Click to download.](#)

- [AgbajeetalChitinESImain.pdf](#)